Fully biosourced amphiphilic block copolymer from tamarind seed xyloglucan and solanesol: synthesis, aqueous self-assembly, and drug encapsulation

Weeranuch Lang[1], Tomohisa Watanabe[2], Chaehun Lee[2], Takayoshi Tagami[3], Feng Li[1], Takuya Yamamoto[1], Kenji Tajima[1], Redouane Borsali[4], Kenji Takahashi[5], Toshifumi Satoh[1,6,*], Takuya Isono[1,*]

[1]Faculty of Engineering, Hokkaido University, Sapporo 060-8628, Japan
[2]Graduate School of Chemical Sciences and Engineering, Hokkaido University, Sapporo 060-8628, Japan
[3]Research Faculty of Agriculture, Hokkaido University, Sapporo 060-8589, Japan
[4]Univ. Grenoble Alpes, CNRS, CERMAV, 38000, Grenoble, France
[5]Faculty of Biological Science and Technology, Institute of Science and Engineering, Kanazawa University, Kanazawa 920-1192, Japan
[6]ICReDD List-PF, Hokkaido University, N21W10, Kita-ku, Sapporo 001-0021, Japan
[7]Department of Chemical & Materials Engineering, National Central University, Taoyuan 320317, Taiwan
[*]Corresponding authors: T. Isono, email address: isono.t@eng.hokudai.ac.jp, tel/fax: +81-11-706-2290; T. Satoh, e-mail address: satoh@eng.hokudai.ac.jp, tel/fax: +81-11-706-6602

Abbreviations: CMC, critical micelle concentration; D_{cal}, theoretical diameter; $Đ$, dispersity (formerly known as polydispersity index); DP, average degree of polymerization; DTG, derivative thermogravimetry; MADLS, multi-angle dynamic light scattering; N_3-Sol, solanesyl 6-azidohexanoate; QC, quercetin; SAXS, small-angle X-ray scattering; XOS_n/XMS_n-*b*-Sol,

xyloglucan oligosaccharide (XOS) and XMS-block-solanesol with n = DP; XOS, xyloglucan oligosaccharide; XOS 7, heptasaccharide; XOS 8, octasaccharide; XOS 9, nonasaccharide

Abstract

This study aims to explore the development of natural bio-based amphiphilic block copolymers for drug delivery applications. We investigated block copolymers derived from tamarind seed xyloglucan and solanesol, focusing on their synthesis, structural analysis, aqueous self-assembly, and drug encapsulation. Specifically, xyloglucan hydrolysate segments with number-average degrees of polymerization (DPs) of between 8 and 44 (XOS_8, XMS_{10}, XMS_{16}, XMS_{28}, and XMS_{44}) were used as the hydrophilic blocks, whereas plant-sourced solanesol was selected as the hydrophobic segment. These two segments were linked *via* click chemistry to create novel XOS-*b*-Sol and XMS-*b*-Sol copolymers, where XOS refers to a xyloglucan oligosaccharide (DP < 10), and XMS denotes a megalosaccharide, defined as a larger xyloglucan polymer with a DP greater than 10. XMS_{10}- and XMS_{16}-*b*-Sol self-assembled in aqueous media to form predominantly narrowly dispersed spherical micelles, while XOS_8-*b*-Sol exhibited a combination of short wormlike structures and spherical micelles. Small-angle X-ray scattering, multi-angle dynamic light scattering, and transmission electron microscopy revealed the XMS_{28}- and XMS_{44}-*b*-Sol micelles are morphologically diverse. XMS_{10}-*b*-Sol solubilized quercetin, a water-insoluble flavonoid, highly effectively, highlighting its potential as an environmentally benign drug carrier.

Keywords: biobased-block copolymers; drug solubilization; self-assembly; solanesol; tamarind seed xyloglucan; xyloglucan megalosaccharide

1. Introduction

Aqueous solutions of amphiphilic block copolymers exhibit diverse self-assembled structures, including spherical, cylindrical, and vesicular morphologies (Giacomelli et al., 2010), and offer unique properties, such as low critical micelle concentrations, drug-encapsulating abilities, and tunable pharmacokinetics (Cabral et al., 2018; Akiba & Sakurai, 2021). In addition, these micelles are also useful in the cosmetics and agricultural fields (Mazzarino et al., 2014; Vega-vásquez et al., 2020). Although synthetic polymers have traditionally dominated such applications, hybrid block copolymers that integrate natural materials, such as lipids, peptides/proteins, and carbohydrates, are gaining attention (Liu et al., 2016; Faisal, S. et al., 2022). These hybrids aim to reduce reliance on petrochemicals and address concerns regarding biocompatibility, biodegradability, and toxicity (Mazzarino et al., 2014; Hato et al., 1999; Halila et al., 2008; Schatz & Lecommandoux, 2010; Alenazi et al., 2023). The pharmaceutical industry is increasingly embracing natural products to mitigate issues related to drug release and side effects (Atanase, 2021). Among hybrid block copolymers, poly-/oligosaccharides have been extensively studied for their synthesis routes and

aqueous self-assembly. Notably, sugar head groups, such as malto-oligosaccharides, cyclodextrins, and dextran, have frequently been linked to various hydrophobic synthetic polymers (e.g., polystyrene, poly(methyl methacrylate), poly(propylene glycol), and polycaprolactone) through diverse chemistries (Giacomelli et al., 2010; Isono et al., 2016). However, sugar-based block-copolymer designs composed entirely of natural products remain limited among current examples, with the exception of a few systems, such as xyloglucan-*b*-peracetylated xyloglucan oligomers (Gauche et al., 2013) and maltoheptaose-*b*-peracetylated maltoheptaose (Modolon et al., 2012).

Hydrophobic (core-forming) blocks need to be carefully selected and designed when developing innovative sugar-based block copolymers exclusively derived from natural sources. The choice of hydrophobic block significantly impacts drug loading and colloidal characteristics. For example, a longer hydrocarbon chain enhances drug-loading capacity by increasing the core size of each micelle (Vinarov et al., 2018) as well as compatibility between the hydrophobic block and the drug structure. Cushen et al. (2014) explored block copolymers composed of oligosaccharides and aliphatic alcohol precursors, such as wax components, but faced water solubility limitations (< 0.1 g/L), which is likely ascribable to the strong hydrophobicity of wax compared to that of the hydrophilic sugar block. Among naturally occurring hydrophobic compounds, fatty acids have emerged as promising alternatives to synthetic hydrophobic blocks (Hato et al., 1999), as evidenced through studies into mannose-based blocks with oleic (Ol) or ricinoleic acid (Ric), with click chemistry used to synthesize $(PMan)_n$-*b*-Ric with n = 3 or 8 (Argudo et al., 2022). Notably, nervonic acid (24:1, MW 366.6) is the longest unsaturated fatty acid, while tetracontanoic acid (40:0, MW 593.1) is the longest saturated fatty acid, where c and d refer to the number of carbon atoms and double bonds, respectively (e.g., c = 24 and d = 1 for nervonic acid) (Piovesana et al., 2021). Similarly, solanesol (45:9, MW 631.1), a coenzyme Q10 precursor from tobacco extract, features a homogeneous long hydrocarbon chain with nine all-trans isoprene units and is a promising alternative to synthetic hydrophobic blocks. Interestingly, while solanesol exhibited well-ordered nanostructures similar to those of synthetic block copolymers in the solid state when conjugated with malto-oligosaccharides *via* click chemistry (Isono et al., 2020; Isono et al., 2022; Chen et al., 2023), their self-assembly behavior in aqueous environments remains unexplored.

The hydrophilic sugar block plays a crucial role in stabilizing the interface between the hydrophobic micelle core and external medium. The properties of the outer shell significantly influence the *in vivo* biodistribution and pharmacokinetic parameters of micelles employed in drug delivery (Allen et al., 1999). Therefore, the sugar block needs to be judiciously selected and cannot be overlooked. The prevalent use of malto-oligosaccharides, specifically starch-based oligomers with average degrees of polymerization (DPs) of seven or less, is ascribable to their good solubilities in various solvents as well as their commercial availability. Synthesizing systems with controlled molar masses are often challenging using other renewable poly-/oligosaccharides that

are poorly compatible with organic solvents (Schatz & Lecommandoux, 2010). Consequently, a significant gap exists in the accumulated knowledge regarding the impact of sugar block length on self-assembly.

In this study, we focused on developing fully bio- and sugar-based block copolymers for aqueous self-assembly using tamarind seed xyloglucan, which is a byproduct of the tamarind pulp industry. This xyloglucan features a cellulose-like β-(1→4)-linked glucan backbone with side chains containing xylosyl and other monosaccharide units such as galactosyl and arabinosyl (Niemann & Carpita, 1997). These side chains suppress cellulose-like chain aggregation and contribute to the amphiphilic character of this xyloglucan, with xylose and arabinose residues exhibiting hydrophobic properties while the galactose residues contribute to its aqueous solubility (Janado & Yano, 1985; Mahajan et al., 2012; Majee et al., 2016). Xyloglucan solutions tend to form precipitates or gel-like structures that depend on factors such as molecular weight, temperature, branching pattern, concentration, and interactions with sugars, alcohols, or polyphenols (Nitta et al., 2004). The smallest repeating units, namely heptasaccharide (XOS 7), octasaccharide (XOS 8), and nonasaccharide (XOS 9), along with xyloglucan megalosaccharides (XMSs; a term introduced by Thoma et al. [1959]) with DPs of 10–100, form the basis of our study (Scheme 1a and b). We recently reported the preparation of a series of XMSs with commercially unavailable DPs *via* enzymatic hydrolysis, and their use in creating a lipid-based micellar solution (Lang et al., 2023a; Lang, et al., 2023b). These XMSs act as cosurfactants alongside Tween 80 and oil owing to their amphiphilic nature, which enabled quercetin (QC), the antioxidant, to be loaded at high levels (Lang, et al., 2023b). The presence of free reducing ends in these moderate-length xyloglucan fragments enables reducing-end-specific modifications ideal for click reactions, aligning with our study's objectives. While other hemicelluloses, such as glucuronoxylan from hardwood, could theoretically provide an adequate amount of reducing ends through partial cleavage, this approach has not yet been explored. Furthermore, tamarind seed xyloglucan provides a well-defined repeating unit structure of XOS 7, 8, and 9 (as noted above), offering a consistent basis for modification and analysis across a range of molecular weights. Our hypothesis in this study revolves around the structural characteristics of xyloglucan oligosaccharides (XOSs) and megalosaccharides (XMSs), including their sizes, sugar components, and shapes, as well as their potential to influence the structures and properties of sugar-based block-copolymer micelles, thereby providing distinctions to their malto-oligosaccharide-derived counterparts.

In this study, we prepared five xyloglucan oligosaccharides and megalosaccharides with number average DPs in 8–44 range (XOS_8-OH, XMS_{10}-OH, XMS_{16}-OH, XMS_{28}-OH, and XMS_{44}-OH), and thoroughly analyzed the molecular structures and thermal properties of the XOSs/XMSs prepared using enzymatic methods. We then synthesized xyloglucan-*b*-Sol as a fully bio-based, sugar-based block-copolymer system that incorporates chemically precise solanesol as a consistent

hydrophobic segment, along with xyloglucan segments with various DPs. Xyloglucan-*b*-Sol was synthesized using a click reaction involving azido-functionalized solanesol (solanesyl 6-azidohexanoate; N_3-Sol) and XOSs/XMSs bearing propargyl groups at their reducing ends (XOS_n/XMS_n-AcC≡CH). Aqueous self-assembly resulted in the formation of micellar aggregates, each with a xyloglucan shell and a solanesol core, which were characterized by size-exclusion chromatography (SEC), multi-angle dynamic light scattering (MADLS), transmission electron microscopy (TEM), and small-angle X-ray scattering (SAXS). We finally showed that poorly water-soluble QC is efficiently solubilized by encapsulation using an aqueous solution of xyloglucan-*b*-Sol.

2. Materials and methods

2.1. Materials

Due to character limitations, the materials used are described in the Supporting Information.

2.2. Preparation of xyloglucan$_n$ segments

Herein, xyloglucan refers to the set of XOS_n-X and XMS_n-X used in this study, where "n" corresponds to the DP of the monosaccharide unit and "X" refers the functional group at the reducing end. XOS_n/XMS_n-OH is referred to as XOS_n and XMS_n in the absence of reducing-end modification. XOS_8-OH is a mixture of $XOS_{7–9}$-OH, and was prepared by fully digesting tamarind seed xyloglucan with *Trichoderma viride* cellulase (Selby & Maitland, 1967). XMS_{10}-OH, XMS_{16}-OH, XMS_{28}-OH, and XMS_{44}-OH were prepared by random digestion for 2 h using the previously reported procedure (Lang et al., 2023a). XOS_8-OH, XMS_{10}-OH, XMS_{16}-OH, XMS_{28}-OH, and XMS_{44}-OH were fractionated by methanol precipitation (60–95%, Table S1), after which the DPs and monosaccharide compositions were analyzed and reported. Here, the peak molecular weights (M_p) and dispersity ($Đ_{SEC}$) of XOS_8-OH, XMS_{10}-OH, XMS_{16}-OH, XMS_{28}-OH, and XMS_{44}-OH were determined to be 1258 ($Đ_{SEC}$ = 1.40), 1566 ($Đ_{SEC}$ = 1.33), 2453 ($Đ_{SEC}$ = 1.63), 4093 ($Đ_{SEC}$ = 2.24), and 6780 Da ($Đ_{SEC}$ = 2.17), respectively, based on SEC in 0.2 M sodium nitrate solution and calibrated against pullulan (see Section 2.4.4 and Table S1). Nanostructures were observed by SAXS (Section 2.4.7), with Guinier analysis performed, and Kratky [$q^2I(q)$ vs. q] and p(r) plots created. The p(r) function, or pair-distance distribution function describes the probability of finding a pair of points within a particle separated by a distance r (Hansen, 2000).

2.3. Synthesis of xyloglucan-*b*-Sol copolymers

Block copolymers were prepared using three sequential reactions (i–iii, Scheme 1) by following previously reported procedures (Isono et al., 2020) with some modifications for high-DP xyloglucan compatibility, notably substituting DMSO for DMF.

2.3.1 Synthesis of propargyl end-functionalized xyloglucan (XOS_n/XMS_n-C≡CH). Following the procedure reported by Halila et al. (2008), the reducing end group of the xyloglucan (XOS_n/XMS_n-OH) was treated with propargylamine (approximately 1.8–2.5 mL/g sugar) under argon for 72 h and 25 °C to yield the xyloglucan-1-propyne derivative (XOS_n/XMS_n-C≡CH). The resulting mixture was added dropwise to ethanol and the precipitate was centrifuged (9,000 ×g, 4 °C for 20 min), collected, and subsequently dried under vacuum overnight.

2.3.2 Acetylation with acetic anhydride (to prevent hydrolysis of the propargyl functional group). The dried precipitate prepared as described above (XOS_n/XMS_n-C≡CH) was fully dissolved in DMSO (dimethyl sulfoxide, approximately 2.5–4 mL/g sugar), after which dehydrated MeOH and acetic anhydride were added to afford a final DMSO:MeOH:acetic-anhydride ratio of 12:8:1 (v/v/v), and the resultant mixture was stirred at 25 °C for 24 h. The reaction was quenched by adding a trace amount of water. The volatiles were evaporated and the residue was added dropwise to ethanol with continuous stirring. The propargyl-end-functionalized xyloglucan (XOS_n/XMS_n-AcC≡CH) was collected following centrifugation and then dried under vacuum. Incorporation of the propargyl group was confirmed by ^{1}H NMR spectroscopy. XOS_8-AcC≡CH, XMS_{10}-AcC≡CH, XMS_{16}-AcC≡CH, XMS_{28}-AcC≡CH, and XMS_{44}-AcC≡CH were obtained in yields of 80, 85, 90, 95, and 98%, respectively, from the corresponding XOS_n/XMS_n-OH.

2.3.3 Click reaction. The xyloglucan-*b*-Sol copolymer was synthesized through the click coupling of N_3-Sol (1.1 eq.) and XOS_n/XMS_n-AcC≡CH (1.0 eq.) catalyzed by CuBr (copper(I) bromide, 0.20 eq.) and PMDETA (*N*,*N*,*N*',*N*'',*N*''-Pentamethyldiethylenetriamine, 1.0 eq.) at 60 °C for 72 h in DMSO at 10% w/v. The reaction was quenched by passing it through a manually packed Amberlite MB-4 column to remove the catalyst followed by ethanol re-precipitation. The block copolymer precipitate was dried overnight under vacuum and traces of unreacted N_3-Sol were eliminated by precipitating the sample from acetone after first dissolving it in water. The complete removal of unreacted N_3-Sol was confirmed by FT-IR. The precipitate was collected, re-dissolved in water, transferred into a dialysis bag, and dialyzed against water to remove residual DMSO and unreacted XOS_n/XMS_n-AcC≡CH, with successful removal verified by SEC. The block copolymer was recovered from the dialysis bag and then passed through a manually packed Amberlite MB-4 column once again to remove any residual catalyst. It was subsequently precipitated in acetone and dried in an oven at 40 °C. The sample was completely ultrasonically dissolved in DMF containing 0.01 M LiCl, filtered, and then subjected to SEC (Fig. S1) using with the same instrument described previously (limit 0.3–10,000 kDa (Isono et al., 2020) to determine the number-average molecular weight ($M_{n,SEC}$) and dispersity ($Đ_{SEC}$) based on polystyrene as the calibration standard.

XOS_8- ($M_{n,SEC}$ = 2200; $Đ_{SEC}$ = 1.05), XMS_{10}- ($M_{n,SEC}$ = 2540; $Đ_{SEC}$ = 1.04), XMS_{16}- ($M_{n,SEC}$ = 3410; $Đ_{SEC}$ = 1.13), XMS_{28}- ($M_{n,SEC}$ = 4580; $Đ_{SEC}$ = 1.21), and XMS_{44}-*b*-Sol were obtained in yields of 60, 65, 68, 70, and 72%, respectively (XMS_{44}-*b*-Sol was not analyzed by SEC owing to its poor solubility). The weight fraction of the xyloglucan segments in the chain (f_{sugar}) was calculated using eq. 1:

$$f_{sugar} = \left(\frac{MW_{XOSn/XMSn-AcC\equiv CH}}{MW_{XOSn/XMSn-AcC\equiv CH} + MW_{N3-Sol}}\right) \quad (1),$$

where $MW_{XOSn/XMSn-AcC\equiv CH}$ (Da) is the sum of the MWs of the propargyl moiety (80 Da) and the sugar M_p obtained by SEC (eluent, 0.1 M $NaNO_3$) (Section 2.4.4), and MW_{N3-Sol} = 770 Da. The MW of xyloglucan-*b*-Sol was determined by summing the sugar M_p (Section 2.4.4), the MW of the azido linker (80 Da), and the MW of N_3-Sol (770 Da). For example, the MW of XOS_8-*b*-Sol = 1260 + 80 + 770 = 2110 Da and $f_{XOS8\text{-}b\text{-}Sol}$ = 1340/(1340 + 770) = 0.64 using eq. (1). Similarly, the MWs of XMS_{10}-, XMS_{16}-, XMS_{28}-, and XMS_{44}-*b*-Sol were determined to be 2400, 3320, 5190, and 7630 Da, respectively, with f_{sugar} values of 0.68, 0.77, 0.85, and 0.90, respectively. MW_{sugar} was assumed to be constant during synthesis.

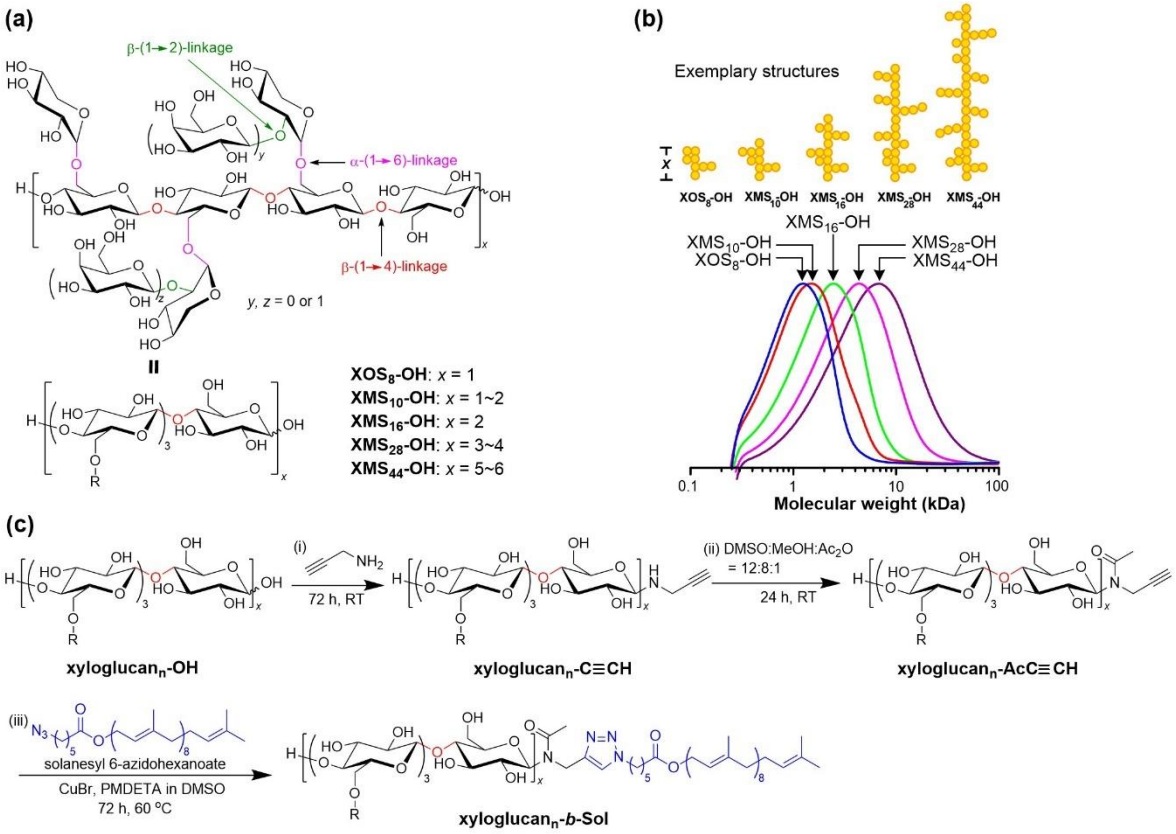

Scheme 1. (a) Proposed structure-forming unit (*x*) of XOSs and XMSs derived from tamarind seed xyloglucan, wherein the β-(1→4)-linked glucopyranose spine is branched with random α-(1→6)-xylosyl and β-(1→2)-galactosyl residues as substituents. XOS_8-OH contains no arabinose residue, while XMS_{10}-OH, XMS_{16}-OH, XMS_{28}-OH, and XMS_{44}-OH are predicted to contain 0.1, 0.2, 0.9, and 3.0 arabinosyl units, respectively, in the chain. (b) SEC analysis (eluent: 0.1 M $NaNO_3$) of five

xyloglucan segments used in this study along with proposed model branch structures with randomly monosaccharide-substituted chains. (c) Synthetic pathway to the xyloglucan-*b*-Sol diblock copolymer, which involves preparing N_3-Sol according to the procedure reported by Isono et al. (2020). (i) Propargyl-functionalization reaction, (ii) acetylation, and (iii) click reaction. "R" represents a xyloglucan side chain involving xylose, galactose, and/or arabinose residues.

2.4. Characterizing xyloglucan-*b*-Sol copolymers and their solution properties

2.4.1. Thermogravimetric analysis (TGA) and Fourier-transform infrared (FT-IR) spectroscopy. Thermal decomposition was examined using a Hitachi STA200RV apparatus. An oven-dried sample (1–3 mg) was placed in an aluminum pan and held at 60 °C for 1 d. TGA was then performed by elevating the temperature to 500 °C at 10 °C/min under N_2, with derivative thermogravimetry (DTG), which involves plotting the first derivative of the TG curve with respect to temperature, subsequently performed. FT-IR spectra were recorded in the 500–4000 cm^{-1} range using a previously described apparatus (Isono et al., 2020).

2.4.2. ^{1}H NMR spectroscopy. Block copolymer structures were characterized by recording ^{1}H NMR spectra on a JEOL JNM-ECS400 instrument (400 MHz) at ambient temperature. The block copolymer was dissolved in DMSO-d_6 to a concentration of 5 g/L, with spectra referenced against the residual protonated solvent peak at 2.50 ppm (Fulmer et al., 2010).

2.4.3. Preparing micelles. Micellar solutions of xyloglucan-*b*-Sol were prepared by dissolving the block copolymer in ultra-pure water at the desired concentration (i.e., 10 g/L or lower) followed by heating at 100 °C for 10 min, and centrifugation at 12,000 ×g for 10 min at 25 °C. Unless otherwise stated, the supernatant was collected for further analysis.

2.4.4. SEC of aqueous $NaNO_3$ solutions. Each XOS_n/XMS_n-OH or xyloglucan-*b*-Sol solution (10 g/L) was diluted with an equal volume of 0.2 M sodium nitrate solution. The resulting solution was subjected to SEC using a high-performance liquid chromatography (HPLC) with a JASCO (Tokyo, Japan) system fitted with two columns in series: 8.0 × 300 mm Shodex OHpak SB-803 HQ (pore size: 1–100 kDa) and 8.0 × 300 mm SB-806 HQ (pore size: 100–20000 kDa). Elution was carried out with 0.1 M sodium nitrate at 0.5 mL/min and 40 °C. Compounds were detected using a refractive index detector (RI 2031 Plus; JASCO, Tokyo, Japan), with calibration performed using Shodex standard P-82 pullulans and maltoheptaose to determine the M_p values (Da) of the sugar and micelle. Elution patterns were primarily used to distinguish between non-self-assembled single-block polymer chains and self-assembled micelles.

2.4.5. Determining critical micelle concentration (CMC) and particle size by MADLS. The pre-determined concentration range for CMCs was evaluated by measuring the scattered light intensities (as kilocounts per second (kcps)) of a series of block-copolymer solution concentration (0.005–10 g/L, 100 µL) at a fixed angle of 173° at 25 °C using a Malvern Zetasizer Nano instrument equipped with a 50 mW frequency-doubled DPSS Nd:YAG laser (λ = 532 nm) (Malvern Panalytical, Ltd., Malvern, UK). The Nile red method provided cross-validation of the CMC. A 500 µM Nile red stock solution in acetone was prepared, and 10 µL was added to vials, allowing the acetone to evaporate in the dark. Block copolymer solutions (1 mL, 0.01–2.0 g/L) were then added to the vials and aged overnight, with measurements performed in two independent experiments. Emission spectra (580–720 nm) were recorded at 25 °C using a Hitachi FP-6500 spectrometer (λ_{ex} = 550 nm). The intensity ratio at 635 nm (hydrophobic) to 660 nm (aqueous) was plotted against concentration (Su et al., 2020). Each CMC was determined as the intersection point of the linear fit obtained from the derived count rate above the CMC and the line corresponding to the averaged plot below the CMC (Vinarov, Katev, Radeva, Tcholakova, & Denkov, 2018). Additionally, the Tyndall effect served as qualitative confirmation when a laser pointer (λ = 532 nm) was directed to observe the scattering of visible light, confirming the presence of colloidal self-assembled structures and the contribution of light scattering effect from XOS_8/XMS_n-OH. For comparison, XOS_8/XMS_n-OH (10 g/L) was tested.

MADLS measurements were performed using an ELSZneo instrument (Otsuka, Tokyo, Japan) with aqueous xyloglucan-*b*-Sol solutions (2 mL) at concentrations of 0.1–5.0 g/L. Scattering angles of 165°, 90°, and 46° were employed, with 25 runs at each angle across three cycles at 25 °C. The hydrodynamic diameter (D_H) was derived from the MADLS autocorrelation function using cumulant analysis software. Zeta potentials were also measured for these samples.

2.4.6. TEM. The block copolymer solution (1 g/L or as stated otherwise) was subjected to TEM using a JEM-2100 transmission electron microscope (JEOL, Tokyo, Japan). A 3-µL droplet of the solution was placed on a carbon-coated copper grid and stained with the equal volume of 2% (w/v) uranyl acetate for 10 s. The diameters of 100 particles were measured using ImageJ software, and the average values were reported. Irregularly shaped NPs were excluded from analysis.

2.4.7. SAXS. SAXS measurements were conducted at the BL40B2 beamline of the SPring-8 facility, Japan, using an incident X-ray-beam wavelength of 0.100 nm. A Pilatus3S 2M detector, positioned 4.0 m from the sample, captured data in the 0.02–2.0 nm^{-1} q range (0.02–10.5 nm^{-1} for xyloglucan-OH). The wavevector magnitude, q, was defined to be: $q = 4\pi/\lambda \sin(\theta)$, where λ is the beam wavelength and 2θ is the scattering angle. Tamarind seed xyloglucan (1 g/L), XOS_8-OH/XMS_n-OH (5 g/L), and the block copolymer solutions (1 g/L) were contained in quartz

capillaries (2-mm diameter, Hilgenberg GmbH) maintained at 25 °C. SAXS data were collected during a 3-min beam-exposure time and processed into one-dimensional $I(q)$ versus q profiles through circular averaging. Background scattering from the solvent and cell was subtracted and the reduced excess scattering intensity was corrected to absolute intensity using water (Milli-Q water) as a standard, following the procedure reported by Xie et al. (2018). Guinier analysis, in which radii of gyration (R_g, nm) were calculated manually, was conducted according to the method of Lang et al. (2023c). The maximum linear dimension of the scattering particle (D_{max}) and the p(r) function plot were computed using the Bayesian IFT method (Hansen, 2000; Jacques et al., 2012) within the BioXTAS RAW 2.2.1 software package (Jacques et al., 2012). Block-component lengths were measured using the Wizard menu in the PyMOL 2.5.5 software package.

Although the scattering pattern for XOS_8-*b*-Sol suggested a predominantly spherical structure, TEM images revealed short worm-like structures. To reconcile these observations, scattering curves for XOS_8-*b*-Sol solutions at 1.0 g/L were fitted using two form factors: a cylindrical core–shell model and a core-shell sphere model, based on a previously reported method with SasView 5.0.6 software (Argudo et al., 2022). In contrast, the core-shell sphere model was exclusively used to fit the scattering curves of XMS_{10}- and XMS_{16}-*b*-Sol solutions.

2.4.8. Determining polarity using a pyrene probe. Polarity was determined using the method described by Lang et al. (2022) with some modifications. A 1 mM pyrene solution in ethanol (10 µL) was added to a 1.0 mM xyloglucan-*b*-Sol solution (990 µL) in a glass cuvette, which was inverted three times to ensure mixing. Pyrene fluorescence at 350–500 nm (λ_{ex} = 335 nm) was recorded immediately using a Hitachi FP-6500 spectrometer at 25 °C, and the ratio of emission intensity at 374 nm (I_1) to that at 385 nm (I_3) was determined. The final pyrene concentration was 10 µM, and the I_1/I_3 ratio value in water was 1.74. The emission intensity was normalized by subtracting the intensity of the block copolymer solution without pyrene and dividing the result by I_3.

2.5. QC solubilization. A 1 g/L solution of xyloglucan-*b*-Sol (100 µL) was thoroughly mixed with excess QC powder (1.0 mg) and then incubated at 25 °C for 6 h (in triplicate), followed by centrifugation 12,000 ×g (3 × 10 min). The supernatant was diluted with DMSO and its absorbance was measured at 381 nm using a UV-visible spectrophotometer (UV1900i, Shimadzu, Tokyo, Japan). The QC concentration of the supernatant was calculated using a calibration plot, and the solubilization capacity of the micelles was calculated using eq. 2:

$$\text{Solubilization capacity (mg QC/g copolymer)} = \left(\frac{S - S_0}{C_0}\right) \qquad (2),$$

where, S is the measured QC solubility (mg/L) in the block copolymer solution, S_0 is the intrinsic solubility of QC in water (mg/L), and C_0 is the concentration of the block copolymer (g/L). We

assumed that no block copolymer was lost during the solubility assay. A portion of the complex supernatant was subjected to SAXS without dilution, with the block copolymer concentration maintained at 1 g/L.

3. Results and discussion

3.1. Preparing five XOS/XMS-OH samples

Tamarind seed xyloglucan was depolymerized *via* fungal cellulase digestion to produce XOS_n-OH and XMS_n-OH. Size fractionation *via* methanol precipitation was controlled by adjusting the volume ratio of methanol to xyloglucan hydrolysate (Lang et al., 2023a). SEC (eluent, 0.1 M $NaNO_3$; pullulan standard) revealed five distinct xyloglucan fractions, XOS_8-OH, XMS_{10}-OH, XMS_{16}-OH, XMS_{28}-OH, and XMS_{44}-OH, with each exhibiting a single peak (Scheme 1b). M_p values ranged between 1260 and 6780 Da with $Đ_{SEC}$ in the 1.33–2.24 range (Table S1). The preparation and isolation methods mirrored those previously reported by Lang et al. (2023b). Compositional analysis revealed that XOS_8-OH, XMS_{10}-OH, XMS_{16}-OH, XMS_{28}-OH, and XMS_{44}-OH have β-D-glucopyranose spines containing 4, 5, 8, 14, and 21 glucosyl units, respectively (Scheme 1b).

The conformations of the native tamarind seed xyloglucan and its five hydrolyzed fragments in aqueous solution were examined using their SAXS intensity profiles (Fig. 1a). As reported by Urakawa et al. (2002), tamarind seed xyloglucan has a strong tendency to laterally aggregate in aqueous solution, with chain stiffness consistent with the assumption that an extended zigzag chain exists, by analogy with cellulose. Consequently, we assumed a rather flat conformation, in which the xylosyl and galactosyl-xylosyl branches extend and fold upright on a cellulose-like flat surface. The SAXS profiles of XOS_8-OH, XMS_{10}-OH, and XMS_{16}-OH show plateaus in their low-q regions, suggestive of the absence of large aggregates and confirming that these sugar chains exist predominantly as individual chains. Conversely, notably higher intensities were observed in the low-q regions of XMS_{28}-OH and XMS_{44}-OH, indicative of possible lateral aggregation, consistent with the report of Urakawa et al. (2002).

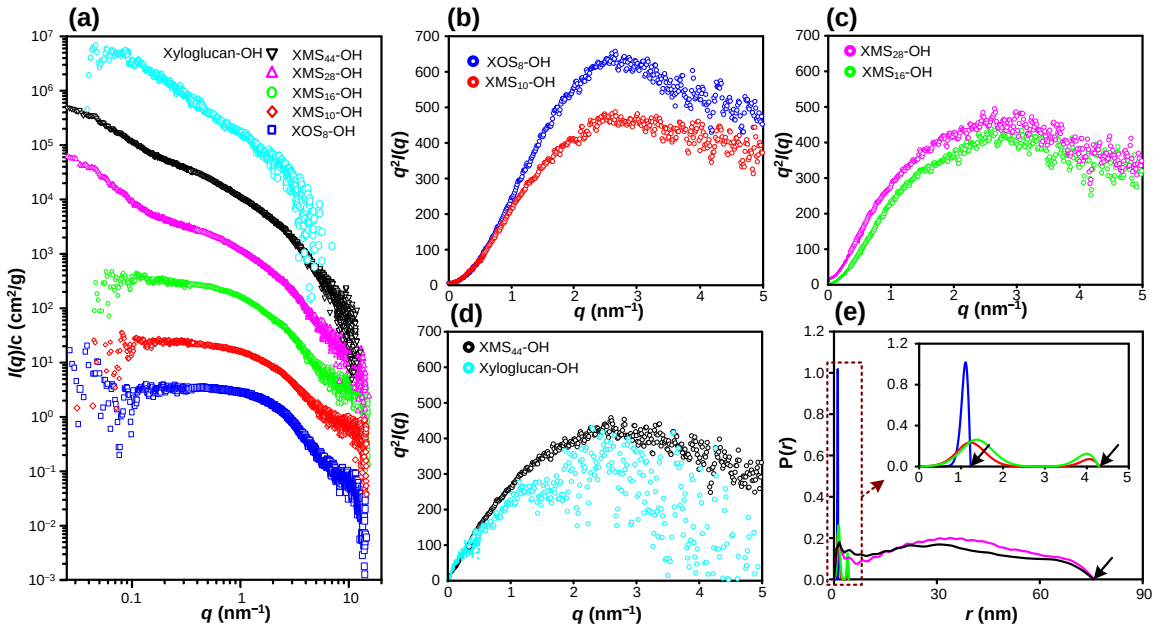

Fig. 1. (a) SAXS profiles of XOS_8-, XMS_{10}-, XMS_{16}-, XMS_{28}-, and XMS_{44}-OH dissolved in water (5 g/L), as well as tamarind seed xyloglucan-OH. Sample data have been scaled by factors of 10, 100, 1000, and 50000, respectively, with those for xyloglucan-OH scaled by 500000 for enhanced clarity. (b–d) SAXS Kratky plots for (b) XOS_8-OH and XMS_{10}-OH, (c) XMS_{16}-OH and XMS_{28}-OH, and (d) XMS_{44}-OH and tamarind seed xyloglucan-OH, and (e) p(*r*) plots for XOS/XMS-OH, with the inset providing a magnified view of the short *r* region. Black arrows indicate D_{max} values.

Kratky plots (Fig. 1b–d) were used to provide further conformational insight. The Kratky plot of XOS_8-OH shows a distinctive characteristic peak at 2.5 nm^{-1}. The characteristic peaks in Kratky plots are related to folded or globular structures; evidently XOS_8-OH has a more isotropic structure that the others (Fig. 1b). The other Kratky plots reveal certain degrees of flexibility with conformations that are not fully extended or completely coiled. Scattering intensity decreases slightly with increasing *q*-value in a manner that corresponds to persistence length, suggestive of semiflexible, ellipsoid, or wormlike chain conformations. This pattern highlights the consistency across all XMS-OH samples, which form anisotropic structures in solution (Urakawa et al., 2002).

The p(*r*) profiles (Fig. 1e) reveal variations in internal structure and size distribution, which enables these cellulase-hydrolyzed samples to be classified into three groups: XOS_8-OH, which has an isotropic shape, XMS_{10}-OH and XMS_{16}-OH with slightly larger cross-sections, and XMS_{28}-OH and XMS_{44}-OH, which tend to aggregate. The p(*r*) function for XOS_8-OH shows a symmetrical peak, consistent with a uniform spherical shape. In contrast, XMS_{10}-OH and XMS_{16}-OH show two separate peaks, suggestive of semiflexible ellipsoidal or worm-like chain conformations, consistent with the report of Urakawa, Mimura, & Kajiwara (2002). XMS_{28}-OH and XMS_{44}-OH exhibited

two peaks at positions similar to those of XMS_{10}-OH and XMS_{16}-OH, which suggests that they have similar molecular-conformational tendencies. However, their broader and more-irregularly shaped p(*r*) functions are consistent with aggregate formation. Urakawa, Mimura, & Kajiwara (2002) provided R_g values of 0.73, 0.72, and 0.72 nm for XOS 7, XOS 8, and XOS 9, respectively while slightly larger values of 1.12 and 1.62 nm were reported for the xyloglucan dimer with a DP of 14–18 and the trimer with a DP of 21–27, respectively. These values are consistent with our results for XOS_8-OH, XMS_{10}-OH, and XMS_{16}-OH, with R_g values determined to be 0.8, 1.2, and 1.5 nm, respectively, by Guinier analysis, whereas their D_{max} values are 1.2, 4.3, and 4.3 nm, respectively, from their p(*r*) profiles. Note that the large R_g values (26.3 and 33.5 nm) for XMS_{28}-OH and XMS_{44}-OH do not reflect their single-molecular dimensions, as they contain larger aggregates. Tamarind seed xyloglucan was determined to have an R_g of 12.4 nm and a D_{max} value of 53.3 nm (Table S2–3). Overall, the XOSs and XMSs prepared in this study have different molecular sizes and shapes, as well as different aggregation tendencies that depend on their DPs, which may affect their block-copolymer self-assemblies.

3.2. Synthesis of xyloglucan-*b*-Sol

Synthesizing a block copolymer *via* azido–alkyne click chemistry requires one polymer to possess an alkyne end group and the other to contain an azido end group (Scheme 1c). To that end, we synthesized two constitutional blocks: azido-functionalized solanesol and a series of propargyl-end-functionalized xyloglucans. The propargyl group was installed on each xyloglucan at its reducing end through direct functionalization involving a reaction with propargyl amine followed by *N*-acetylation, thereby eliminating the need for protection/deprotection chemistry (Halila et al., 2008), to give XOS_8-AcC≡CH, XMS_{10}-AcC≡CH, XMS_{16}-AcC≡CH, XMS_{28}-AcC≡CH, and XMS_{44}-AcC≡CH. DMSO was selected as the solvent (instead of commonly used solvents, such as tetrahydrofuran (THF), DMF, and MeOH) for reactions (ii) and (iii) in Scheme 1c because it ensured homogeneous reaction conditions. Excess N_3-Sol was used in reaction (iii) to guarantee complete conversion, with any free N_3-Sol easily removed by reprecipitation from acetone, which simplified the purification process compared to the sugar-purification protocol reported by Plucinski, Willersinn, Lira, Dimova, & Schmidt (2020) that requires the use of azido-functionalized PS-resin.

We used FT-IR and ^{1}H NMR spectroscopy to further confirm that covalent bonds had formed between the xyloglucan and solanesol blocks. The FT-IR spectrum of xyloglucan-*b*-Sol displayed in Fig. 2a reveals a new absorption peak at 1730 cm^{-1} that is attributable to the ester C=O group in the hexanoate linker of N_3-Sol. The lack of a signal at 2097 cm^{-1}, which is indicative of the azido group (N_3) in N_3-Sol, suggests the click reaction involving XOS_n/XMS_n-AcC≡CH had been successful. The ^{1}H NMR spectra of the block copolymers dissolved in DMSO-d_6 (Fig. 2b and

Fig. S2) reveal characteristic signals at 7.78 and 8.06 ppm attributable to the triazole junction resulting from click coupling between N_3-Sol and XOS_n/XMS_n-AcC≡CH, consistent with previous reports (Isono et al., 2020). Weight fractions were calculated using theoretical values derived from eq. 1, which revealed f_{sugar} values of 0.64–0.90 (Table 1).

TGA was used to examine thermal stability, the results of which are shown in Fig. S3, with corresponding thermal-decomposition temperatures at 5% weight loss ($T_{d,5\%}$) and DTG peak-top value ($T_{d,DTG}$) listed in Table S4. While XOS_8-*b*-Sol exhibited a slightly higher $T_{d5\%}$ value compared to the corresponding unmodified XOS_n/XMS_n-OH (254.7 vs. 253.8 °C) the other samples exhibited lower values (Fig. S3c). The heat-degradation profiles in Fig. S3d reveal that the $T_{d,DTG}$ value of the block copolymer shifts closer to that of XOS_n/XMS_n-OH with increasing sugar content.

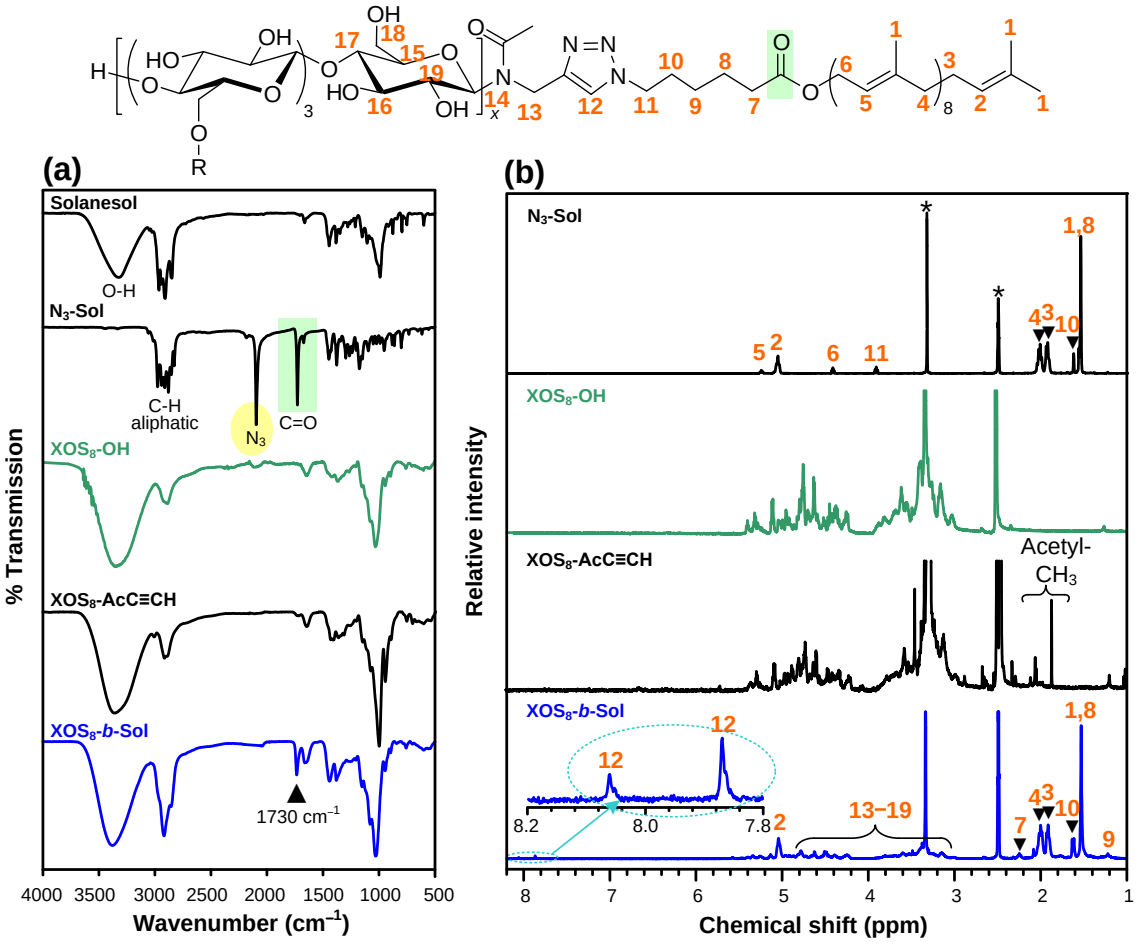

Fig. 2. Structural characterizing XOS_8-*b*-Sol, a representative example of the five prepared xyloglucan-*b*-Sol samples. (a) Comparing the FT-IR spectra XOS_8-*b*-Sol and its relevant reactants. Arrowheads indicate signals corresponding to linker bonds. (b) ^{1}H NMR spectra of XOS_8-*b*-Sol and its relevant reactants acquired in DMSO-d_6. The asterisks indicate residual solvent peaks.

Table 1. Physicochemical properties of the five xyloglucan-*b*-Sol samples

Copolymer	MW[a]	f_{sugar}[b]	CMC [c] (g/L)	CMC [c] (μM)	I_1/I_3 ratio	D_H [d] (nm)	D_{TEM} (nm)	Self-assembled major structure in water
XOS_8-*b*-Sol	2110	0.64	0.09 ± 0.01	40.3 ± 3.4	1.09 ± 0.02	12.7	13.2	Spherical/short-worm
XMS_{10}-*b*-Sol	2400	0.68	0.10 ± 0	41.7 ± 0	1.12 ± 0.02	10.4	15.0	Spherical
XMS_{16}-*b*-Sol	3320	0.77	0.12 ± 0.14	42.2 ± 8.5	1.07 ± 0.03	13.3	16.6	Spherical
XMS_{28}-*b*-Sol	5190	0.85	0.30 ± 0.28	53.0 ± 6.8	1.13 ± 0.07	19.7	13.4	Spherical/anisotropic-object
XMS_{44}-*b*-Sol	7630	0.90	0.50 ± 0.42	60.3 ± 7.4	1.07 ± 0.03	55.6	14.3 [e]	Spherical/anisotropic-object

[a] Average value [b] Weight fraction of xyloglucan in the copolymer chain calculated using eq. 1. [c] The CMC values were determined using the Nile red assay. [d] Values obtained from the number-based distribution size using MADLS at 165° (Fig. 4c). [e] Only spherical particles were measured, as described in Section 2.4.6.

3.3. Self-assembling xyloglucan-*b*-Sol in water

All xyloglucan-*b*-Sol samples were soluble in water when heated at 100 °C, with only XMS_{28}- and XMS_{44}-*b*-Sol showing slight cloudiness at a concentration of 10 g/L. Pyrene was used to evaluate solution polarity. A shift in the I_1/I_3 ratio from that of a polar environment (water: 1.74) indicates that the fluorescence probe interacts with the hydrophobic solanesol segment. All five block copolymers exhibited comparable I_1/I_3 ratios of 1.07–1.13, as summarized in Table 1. Micelle formation in an aqueous medium was further verified by SEC (eluent: 0.1 M $NaNO_3$), as shown in Fig. 3. XOS_8-*b*-Sol and XOS_{10}-*b*-Sol only exhibited elution peaks in the high molar-mass region (equivalent to 73 and 113 kDa pullulans, respectively), which is ascribable to self-assembled micelles, while each remaining block copolymer exhibited two elution peaks, one in the low molar-mass range (3.4–7.3 kDa) ascribable to non-self-assembled single block polymer chains, and the other in the high molar-mass range (151–266 kDa) that corresponds to self-assembled micelles. The single-polymer-chain peak area was observed to increase to 10%, 20%, and 42% with increasing f_{sugar} (XMS_{16}-, XMS_{16}-, and XMS_{44}-*b*-Sol, respectively); however, these peak areas may not fully represent the actual ratios of self-assembled versus unassembled chains in water due to potential shear effects during SEC measurements. This distinction is particularly relevant as it was not observed for copolymers with short sugar blocks, such as XOS_8- and XMS_{10}-*b*-Sol (f_{sugar} = 0.64 and 0.68, respectively), and was negligible for XMS_{16}-*b*-Sol (f_{sugar} = 0.77).

The CMC marks the point at which amphiphilic molecules, including block copolymers, begin to aggregate to form micelles. CMCs were determined by measuring the light-scattering intensities of a series of differently concentrated block-copolymer solutions (Zepon et al., 2015). Based on the SEC results presented above, we initially expected CMC to simply increase with increasing f_{sugar}; that is, increasing the length of the hydrophilic segment at a fixed hydrophobic-block length was expected to increase the CMC. However, Fig. S4a–f reveals an interesting trend: the CMC increased in moving from XOS_8-*b*-Sol to XMS_{16}-*b*-Sol, whereas it decreased with further increases in f_{sugar}. The significantly lower CMC values of XMS_{28}- and XMS_{44}-*b*-Sol are attributable to the strong aggregation tendencies of their long XMS chains, as discussed in Section 3.1. Because light-scattering intensity is more sensitive to larger aggregates than smaller micelles, the CMC values obtained using this technique may not accurately reflect the actual micelle-forming abilities of compounds that tend to aggregate. In fact, the SEC result for XMS_{44}-*b*-Sol shown in Fig. 3a reveal that 42% of the block-copolymer molecules are molecularly dissolved, which is inconsistent with it exhibiting the lowest CMC value among the block copolymers examined. Consequently, the self-assembly behavior of the present block-copolymer system is not only affected by the hydrophilic/hydrophobic balance but also by the inherent properties of the XMS segment. The Tyndall effect shown in Fig. S4g confirmed the scattering of pure XOS_8/XMS_n-OH, highlighting the significant contribution of the hydrophilic XOS_8/XMS_n domain to the overall assembly. The

Nile Red assay was utilized to cross-validate CMC determination, leveraging the fluorescence enhancement of Nile Red when interacting with hydrophobic domains formed above the CMC. As shown in Fig. 3b, the emission spectra at 0.2 g/L block-copolymer solution reveal distinct patterns, with XMS$_{44}$-*b*-Sol exhibiting the broadest and lowest intensity emission along with an upturn at lower emission wavelengths. This characteristic becomes more pronounced at higher concentrations, as depicted in Fig. S5, compared to other block copolymers. The CMC determination for XMS$_{10}$-*b*-Sol is provided as a representative example in Fig. 3c, with detailed data for other block copolymers shown in Fig. S6. The CMC values, summarized in Table 1, follow a trend based on the weight fraction of the xyloglucan segment (Fig. 3d). This correlation underscores the critical role of the hydrophilic segment in determining the concentration threshold for self-assembly.

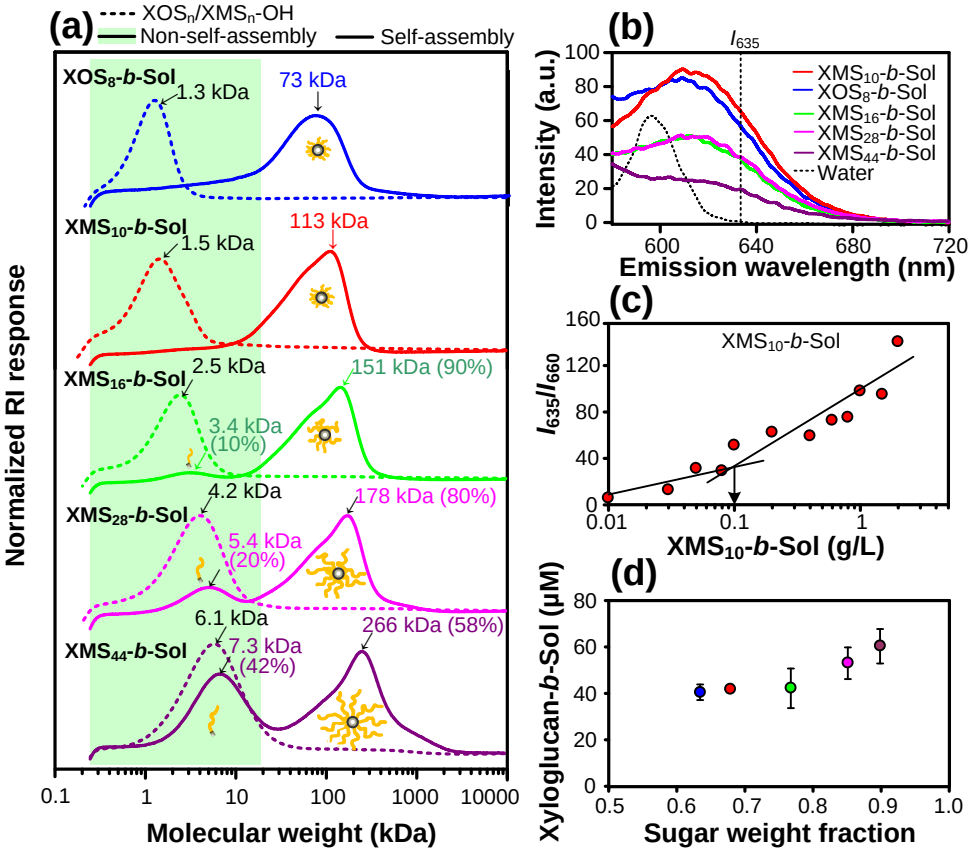

Fig. 3. (a) SEC traces for the five xyloglucan-b-Sol samples, separated using sequential Shodex OHpak SB-803 HQ (1–100 kDa) and SB-806 HQ (100–20,000 kDa) HPLC columns with 0.1 M sodium nitrate as the mobile phase. The traces exhibit bimodal distributions, representing free copolymer chains (non-self-assembled, smaller molecular weight peak, slightly larger than XOS$_8$/XMS$_n$-OH) and primary micelles or clusters (larger molecular weight peak). (b) Emission spectra of Nile red (5 μM) in the presence of xyloglucan-*b*-Sol samples at 0.2 g/L. The dashed line represents Nile red in water (control), indicating no self-assembly. Emission intensity at 635 nm was used to determine CMC values, exemplified for XMS$_{10}$-*b*-Sol in (c). The arrow indicates the

CMC, with other samples detailed in Fig. S6. (d) CMC values (in μM) as a function of sugar weight fraction.

3.4. Micellar nanostructural analysis

A single glucose residue is about 0.6 nm long. Assuming that the repeating subunits consist of four fully extended glucose units in the spine, its total length should be four-times that of Glc (i.e., 2.4 nm), which is slightly less than that of fully extended N_3-Sol (3.8 nm), resulting in a theoretical diameter (D_{cal}) of 12.4 nm for a XOS_8-*b*-Sol micelle, assuming a core–shell spherical micellar structure in water, as an example (Scheme 2). Similarly, the total lengths of the β-(1→4)-spine for XMS_{10}-, XMS_{16}-, XMS_{28}-, and XMS_{44}-*b*-Sol, assuming spinal glucose numbers of approximately 5, 8, 14, and 21 units, were calculated, which led to predicted D_{cal} values of 13.6, 17.2, 24.4, and 32.8 nm, respectively.

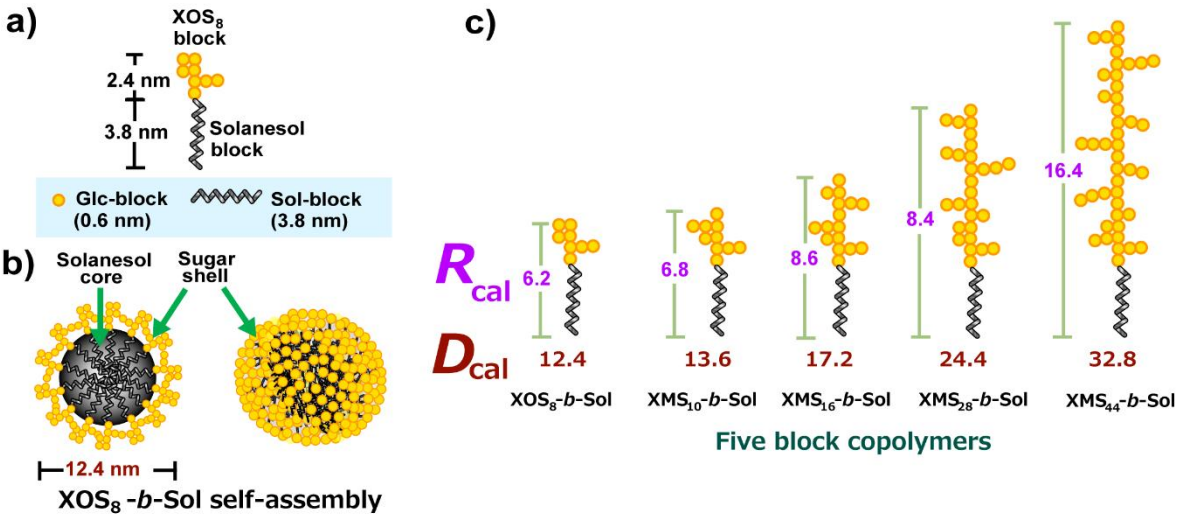

Scheme 2. (a) Model used to predict the length of a single XOS_8-*b*-Sol segment, which self-assembles in water to form a spherical micelle, with (b) cross-sectional and surface views. The β-(1→4)-glucopyranosyl unit is predicted to be 0.6 nm long. N_3-Sol is 3.8 nm long; when combined with the branched structure of the XOS_8 block provides a calculated radius (R_{cal}) of 6.2 nm and a diameter (D_{cal}) of 12.4 nm. (c) R_{cal} and D_{cal} values calculated for XMS_{10}-, XMS_{16}-, XMS_{28}-, and XMS_{44}-*b*-Sol in a similar manner.

Micelles were characterized using 1 g/L MADLS and TEM (Fig. 4); DLS was used to determine the D_H values of particles in solution by comparing the decay rates of autocorrelation functions at different angles, primarily at 165° (Fig. 4a) and 46° (Fig. 4b), whereas TEM provided high-resolution images than enabled visualization of the micellar morphology of the dry state. Detailed particle dynamics are discernable in Fig. 4a–b. The autocorrelation functions at 165° of spherical structures, such as the XOS_8-, XMS_{10}-, and XMS_{16}-*b*-Sol micelles, decayed uniformly

548 across all angles, indicative of consistent size distributions; they were also consistent for XMS_{10}-
549 and XMS_{16}-*b*-Sol at 46°. However, XOS_8-*b*-Sol exhibited a broader decay curve, with TEM (Fig.
550 4g) confirming the co-existence of wormlike structures, which is possibly ascribable to the
551 hydrophilic/hydrophobic balance in this system. The relatively short XOS_8 chain does not
552 sufficiently isolate the hydrophobic core from water, whereas XMS_{10} and XMS_{16} effectively
553 stabilize micelles by adequately covering their surface. Similar patterns have been observed for
554 other systems. For example, Dal Bó et al. (2012) found that shorter PEG600 shells led to a
555 vesicular morphology, while the longer hydrophilic segments of the PEG900 glycoconjugates
556 resulted in highly regular spherical micelles. XMS_{28}-*b*-Sol and XMS_{44}-*b*-Sol exhibited varying
557 decay rates, particularly at 46°, indicative of anisotropic structures. The XMS_{28}-*b*-Sol and XMS_{44}-
558 *b*-Sol samples exhibited bimodal intensity-weighted DLS size distributions (Fig. 4e–f), and TEM
559 images (Fig. 4j–k) revealed larger structures, including spheres and rods that correspond to the
560 larger size populations in the intensity-weighted DLS size distributions. The formation of large and
561 irregularly shaped aggregates may be associated with the propensity of long sugar chains to
562 aggregate, as previously mentioned, consistent with the SAXS data shown in Fig. 1. Consequently,
563 the mechanism responsible for the formation of such anisotropic structures from XMS_{28}- and
564 XMS_{44}-*b*-Sol is distinctly different from that associated with the formation of the wormlike
565 structure observed for XOS_8-*b*-Sol.

566 The sphere sizes observed in DLS measurements, particularly in the number- and intensity-
567 based distributions, appear more consistent with the expected size progression as sugar length
568 increases, compared to the sizes observed in TEM (Table 1). TEM in Fig. 4g–k revealed that XOS_8-,
569 XMS_{10}-, and XMS_{16}-*b*-Sol have TEM-determined sizes (D_{TEM}s) that are consistent with the DLS
570 data, whereas those determined for XMS_{28}-*b*-Sol and XMS_{44}-*b*-Sol do not match the longer lengths
571 of these sugars. The TEM images distinctly display gaps between the XMS_{28}-*b*-Sol and XMS_{44}-*b*-
572 Sol micelles at a high concentration of 10 g/L (Fig. S7) because the electron contrast is insufficient
573 to detect long sugar chains. Nevertheless, the particles remained separated, most likely due to the
574 larger sugar shells associated with XMS_{28} and XMS_{44}. This suggests that a thicker shell layer forms
575 with increasing sugar-segment DP, compared to those of XOS_8-, XMS_{10}-, and XMS_{16}-b-Sol. The
576 discrepancy between the sizes of the isolated XMS_{28}-*b*-Sol spherical micelles determined by DLS
577 and TEM is rationalized by micelle shrinkage during the drying process used to prepare the TEM
578 samples. Meanwhile, the large difference in D_H and D_{TEM} recorded for XMS_{44}-*b*-Sol is possibly
579 attributable to the coexistence of spherical micelles and larger irregularly shaped structures. DLS
580 provided average information for coexisting structures, while only the regular spherical micelles
581 were counted when determining D_{TEM}.

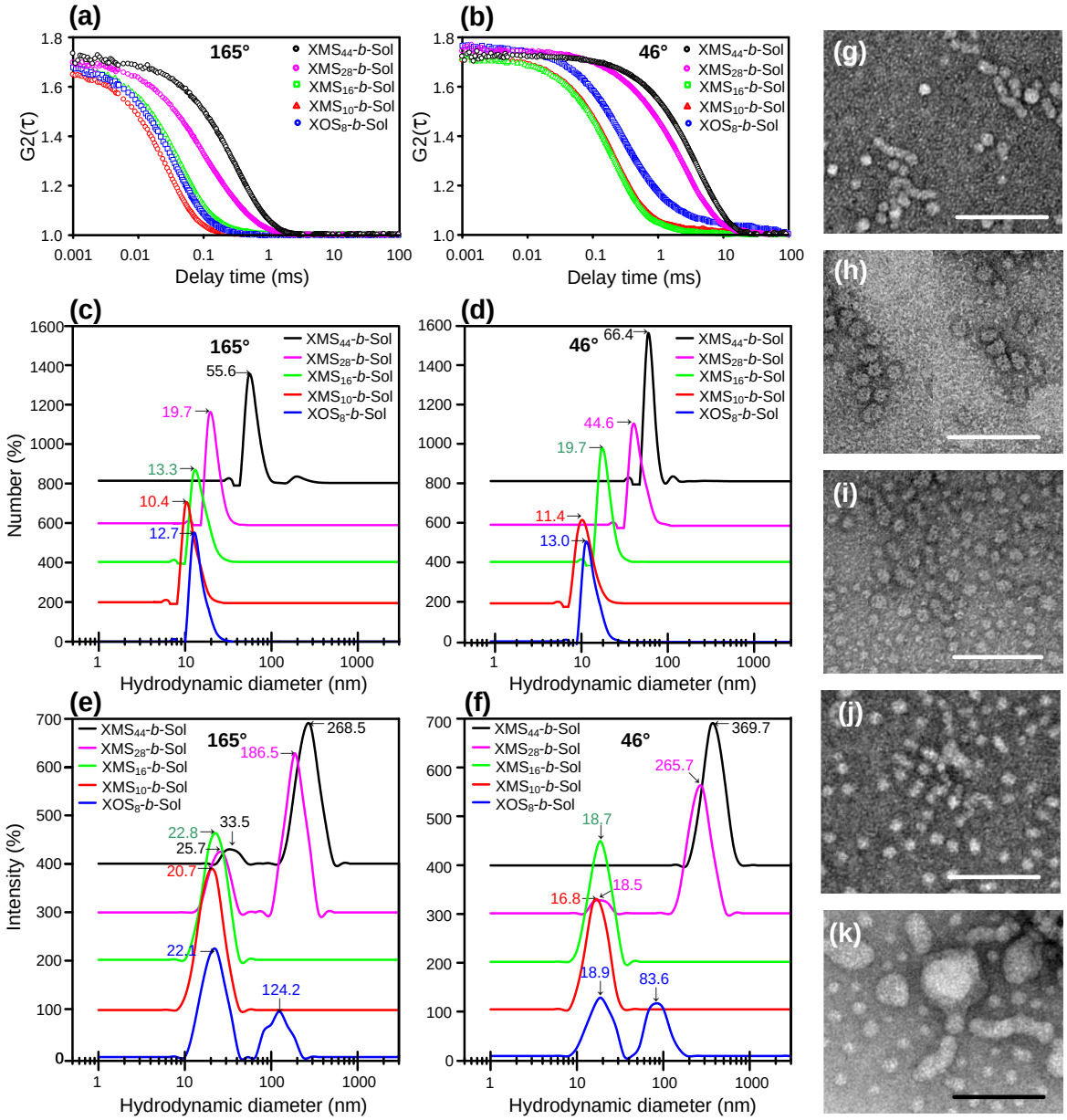

Fig. 4. Autocorrelation functions for the five xyloglucan-*b*-Sol samples acquired at scattering angles of (a) 165° and (b) 46°. Number-based size distributions at (c) 165° and (d) 46°, and intensity-based size distributions at (e) 165° and (f) 46°. TEM images of negatively stained 1 g/L copolymer solutions of (g) XOS_8-*b*-Sol, (h) XMS_{10}-*b*-Sol, (i) XMS_{16}-*b*-Sol, (j) XMS_{28}-*b*-Sol, and (k) XMS_{44}-*b*-Sol (scalebars: 100 nm).

The self-assembled nanostructures were further examined using solution SAXS (Fig. 5a); XOS_8-, XMS_{10}-, and XMS_{16}-*b*-Sol exhibited similar scattering curves, each with a plateau at around 0.1–0.2 nm^{-1}, which suggests that the majority of scatterers are spherical.

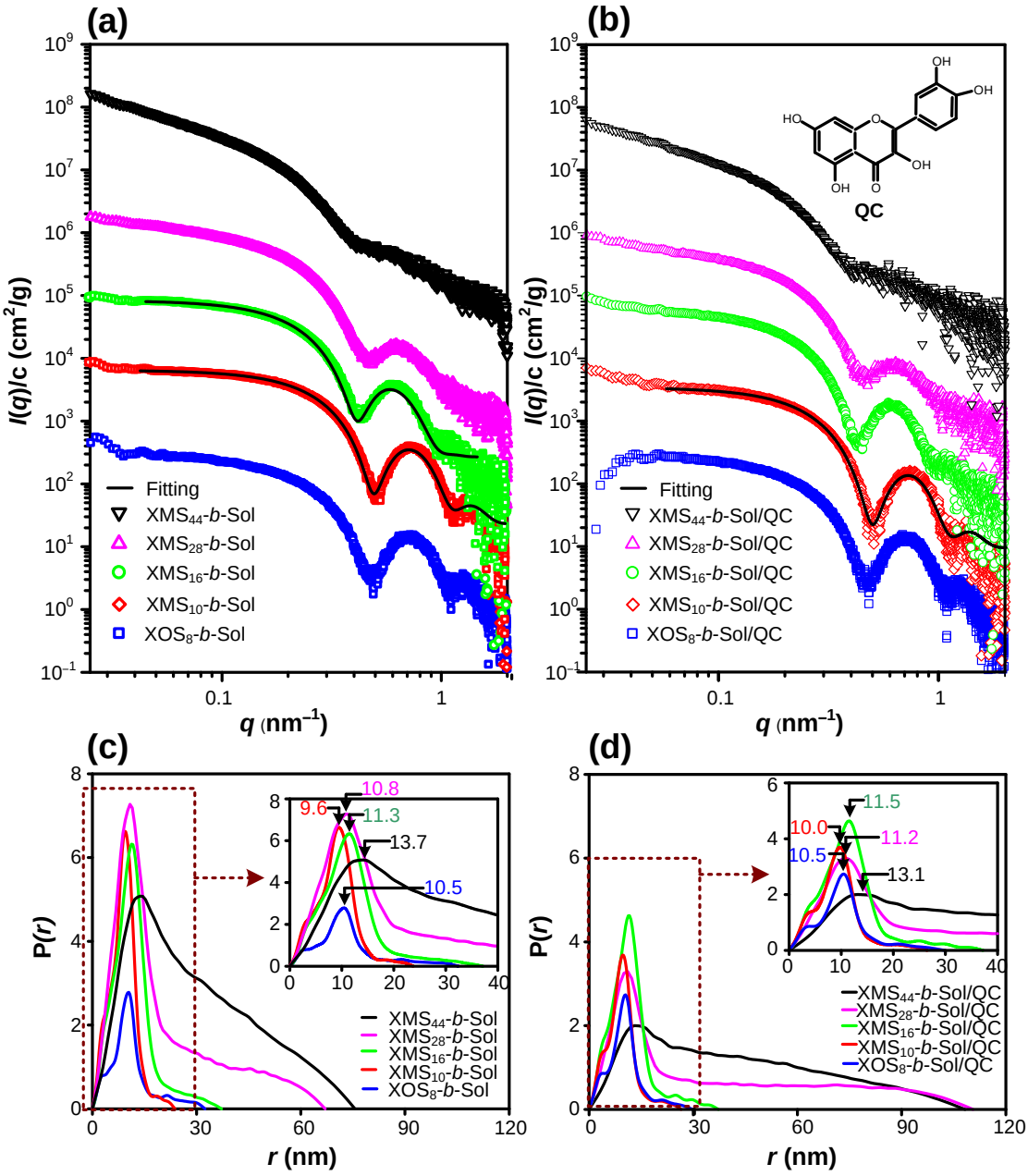

Fig. 5. (a) SAXS profiles of 1 g/L solutions of XOS_8-, XMS_{10}-, XMS_{16}-, XMS_{28}-, and XMS_{44}-*b*-Sol obtained, with fitted curves for XMS_{10}- and XMS_{16}-*b*-Sol determined using the spherical core–shell model. (b) Scattering curves for XOS_8-, XMS_{10}-, XMS_{16}-, XMS_{28}-, and XMS_{44}-*b*-Sol-encapsulated QC, including the fitted curve for QC-incorporated XMS_{10}-*b*-Sol. Curves were scaled by factors of 10, 100, 1000, and 50000, respectively, for enhanced clarity. A combination of panels (a) and (b) is shown in Fig. S8. (c–d) p(*r*) plots corresponding to panels (a–b), with insets providing magnified views in the short *r* region. The *r* values corresponding to the highest p(*r*) peaks are indicated in the inset.

The scattering curve for XMS_{44}-*b*-Sol (f_{sugar} = 0.90), the copolymer with longest sugar blocks in this study, shows a steady increase in scattering intensity in the low-*q* region ($q < 0.1$ nm^{-1}), consistent with different morphologies and larger micelles compared to those with shorter sugar blocks. The *q* power law of −1.6 for XMS_{44}-*b*-Sol in the low *q* region is suggestive of more anisotropic shapes than spherical ones and/or a higher population of such structures, consistent with the diverse aggregate morphologies observed by TEM. The broad p(*r*) function and large D_{max} also contribute to shape anisotropy (Fig. 5c). XMS_{28}-*b*-Sol exhibited a similar trend, albeit to a lesser extent, to that observed for XMS_{44}-*b*-Sol. Notably, all scattering curves displayed distinct oscillations. A general trend of a lower *q* shift in the first minimum position was observed with increasing sugar-block length, suggestive of an increase in the size of the correlated structures. A decrease in oscillation depth with increasing sugar-block length is another notable trend, indicative of increasing structural dispersity. These findings are consistent with the DLS and TEM results that showed that XMS_{10}- and XMS_{16}-*b*-Sol formed well-defined micelles, whereas XMS_{28}- and XMS_{44}-*b*-Sol exhibited different morphologies. XOS_8-*b*-Sol clearly exhibited wormlike micelles by TEM (Fig 4g); however, this was not observed in the corresponding SAXS profile (e.g., a steady increase in scattering intensity in the low-*q* region), which suggests that the majority of XOS_8-*b*-Sol forms spherical micelles with a low proportion of wormlike micelles present.

Assuming a fully extended solaneol-block chain in the core of the spherical micelle, all block copolymers have identical core radii; however, they should exhibit different shell thicknesses, as shown in Scheme 2. Quantitative SAXS experiments can provide additional insight into the structures of micelles. We firstly fitted data according to the model for truly monodispersed systems, with XMS_{10}- and XMS_{16}-*b*-Sol well fitted using a spherical core–shell model, as shown in Fig. 5a, with corresponding data summarized in Table S5. As expected, the solanesol-core radius remained consistent at 3.8 nm. The shell of the XMS_{10}-*b*-Sol micelle was 2.6 nm thick, while that of the XMS_{16}-*b*-Sol micelle was 4.5 nm thick; both values are consistent with the predicted lengths shown in Scheme 2. For XOS_8-*b*-Sol, fitting was performed using both cylindrical and spherical core–shell models with individual fits as shown in Fig. S9. Neither model fully captured the system, as evidenced by moderately high chi-square values (χ^2 = 67.0 and 68.2, respectively), likely due to the coexistence of two micelle populations, as discussed earlier.

3.5. Solubilizing QC

The level of QC in blood plasma is less than 1% of the intake level because it is almost insoluble in water (0.17–7.7 μg/mL) and is poorly permeable (Gao et al., 2009). In this study, the solubility of QC in water was measured to be 4.7 μM or 1.4 μg/mL. Traditional methods for enhancing the bioavailability and effectiveness of water-insoluble active pharmaceutical ingredients involve forming complexes with compounds such as cyclodextrins or polymers (Bhalani et al., 2022). This

technique improves solubility by altering the crystal lattice structure or forming soluble complexes. In our previous study, isolated XMS-OH segments exhibited the potential to solubilize poorly water-soluble bioactive compounds, such as curcumin and QC, and the degree of solubilization was found to increase linearly with the concentration of the XMS-OH segments (Lang et al., 2023a; Lang et al., 2023b). Studies with XMS_{16}-OH and XMS_{56}-OH have shown that hydrophobic interactions between QC and the XMSs lead to significantly improved solubilities, with enhancements of up to 4.8- and 5.8-fold observed with specific XMS-OH solutions at 100 g/L (Lang et al., 2023b). Inspired by these results, we explored the potentials of XOS_8-, XMS_{10}-, XMS_{16}-, XMS_{28}-, and XMS_{44}-*b*-Sol to enhance QC solubility. Drugs can be encapsulated in micelles during their formation or subsequently, with preparation methods recently reviewed by Ghezzi et al. (2021), which revealed that the direct dissolution of both components in their solid forms was the easiest, while other methods involve dialysis, emulsion with solvent (or co-solvent) evaporation, and solution casting followed by film hydration. In this study, we prepared the soluble complex using a simplified method involving pre-dissolved low concentrations of block-copolymer solutions (1 g/L). The drug was incorporated at the maximum capability of each block-copolymer micelle, with excess drug remaining in its water-insoluble state removed by centrifugation. We observed significant improvements in QC solubility compared that observed in water (Fig. 6a), which indicates that the hydrophobic solanesol cores of these block-copolymer micelles are essential for enhancing solubility. XMS_8- and XOS_{10}-*b*-Sol exhibited the most notable solubilization capacities for QC, with all samples enhancing QC solubility by more than a factor of ten compared to its solubility in water. In contrast, XMS_{28}- and XMS_{44}-*b*-Sol were the least effective among the copolymer solutions, with five-to-six-fold increases in efficacy observed, which is likely due to non-micelle-forming chains binding to the drug *via* hydrophobic interactions, which is significantly less effective than encapsulation within the core of the micelle. Nevertheless, this block copolymer system provides an overall more effective binding environment for QC, resulting in a notably higher solubilization capacity compared to XMS-OH. Thus, while both XMS-OH and XMS-*b*-Sol improve QC solubility, the XMS-*b*-Sol micelles demonstrate superior performance due to their self-assembly into micellar structures, which encapsulate QC more efficiently.

XMS_{10}- and XMS_{16}-*b*-Sol were previously recognized as having uniform spherical micellar structures. The TEM images in Fig. 6c revealed that XMS_{10}-*b*-Sol has the most uniform shape following QC encapsulation and the maximum solubilizing capacity of 13.6 ± 0.9 mg/g (Fig. S10). On the other hand, XMS_{16}-*b*-Sol unexpectedly exhibited cylindrical shapes, which is rationalized by the incorporation of the drug altering its hydrophobic/hydrophilic balance.

It would be interesting to determine whether such effective drug solubilization can be achieved by simply adding QC into micelle solutions. One might expect that this technique may not

successfully encapsulate owing to the strongly hydrophobic core. Zatorska-Plachta et al. (2021) addressed this issue when attempting to load curcumin into poly(styrene)-*b*-poly(acrylic acid) micelles. The high glass transition temperature (T_g) of polystyrene (~100 °C) resulted in micellar cores that were frozen at room temperature, which hindered curcumin penetration. However, our method effectively addresses this issue because the solanesol core has a low T_g (−77.1 °C) (Isono et al., 2020), which endows the micelle with dynamic behavior that enables the drug to be incorporated within the hydrophobic core, resulting in promising outcomes when the drug is mixed with a predissolved block-copolymer solution.

SAXS intensity profiles were acquired during QC incorporation to obtain detailed information on QC localization within the internal structure. Fig. 5b shows that, with the exception of XOS_8-*b*-Sol, all samples exhibited somewhat lower scattering intensities. The monodispersed XMS_{10}-*b*-Sol system was subjected to SAXS model-fitting using the spherical core–shell form factor (Fig. 5b, Table S3), which revealed that QC molecules are likely to be located in the core of XMS_{10}-*b*-Sol as the inner core radius was observed to change to 4.0 nm (from 3.8 nm) while shell thickness remained unchanged. These results highlight the critical roles that micellar interactions play when designing drug-delivery systems. Although traditional micellar interactions are crucial to effectively solubilize most block copolymers, XMS_{28}- and XMS_{44}-*b*-Sol may not provide the same advantages for drug encapsulation within micelles owing to their lower populations of micelle-forming chains, which underscores the importance of selecting an appropriate sugar chain length to effectively maintain micellar interaction mechanisms in pharmaceutical formulations and drug-delivery systems.

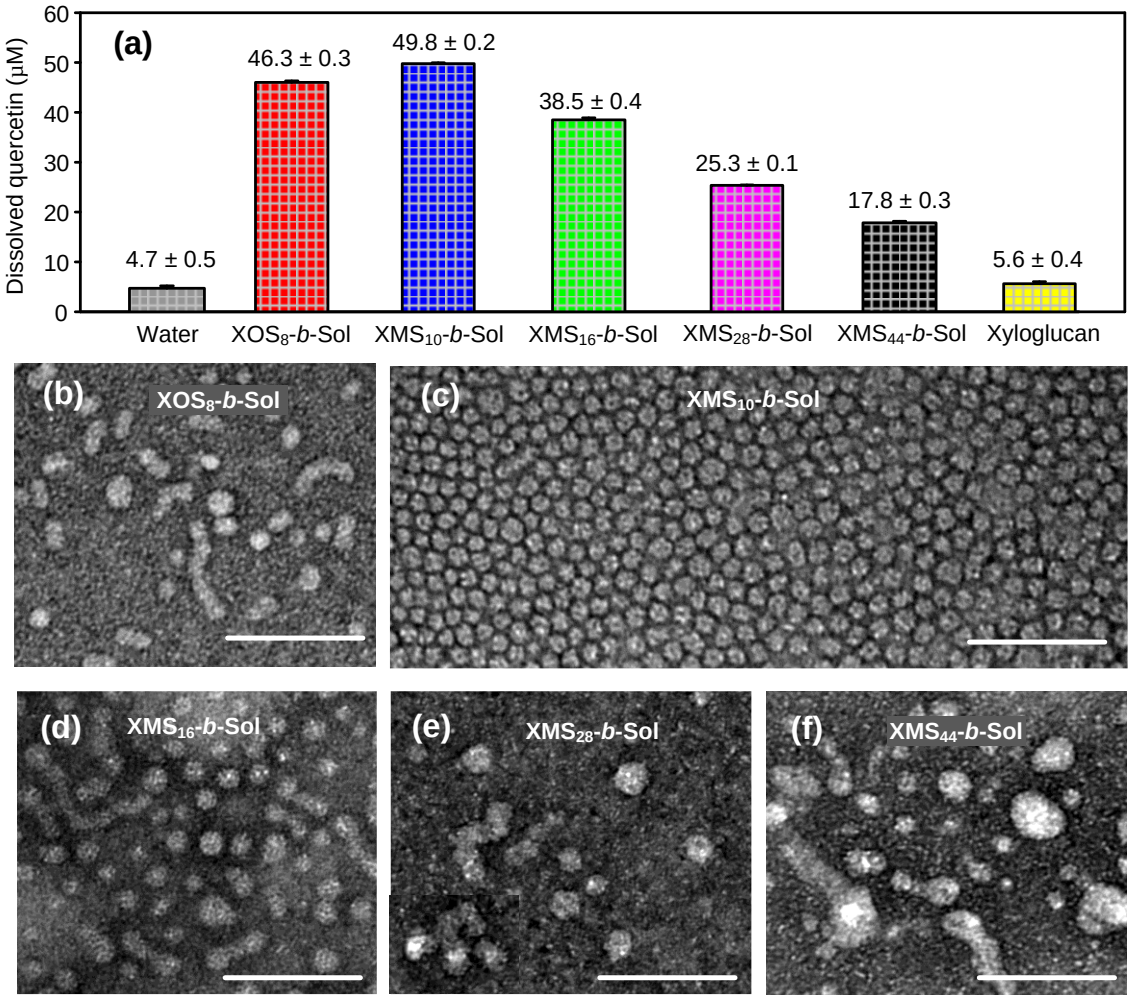

Fig. 6. (a) Water solubilities of QC upon its addition to 1 g/L copolymer and tamarind seed xyloglucan solutions at 25 °C. (b–f) TEM images of QC complexed with XOS_8-, XMS_{10}-, XMS_{16}-, XMS_{28}-, and XMS_{44}-*b*-Sol, respectively, using 1 g/L block-copolymer solutions. Scalebars: 100 nm.

4. Conclusion

In this study, we chemically coupled solanesol, a plant-based substance with unconventional xyloglucan segments obtained from tamarind seeds, to form novel bio-based block copolymers. Block-copolymer self-assembly in aqueous media resulted in the formation of spherical micelles and wormlike structures, depending on the length of the sugar block. Long sugar blocks possibly resulted in more molecularly dissolved non-self-assembled block-copolymer chains in water. Notably, XMS_{10}- and XMS_{16}-*b*-Sol, with f_{sugar} values of 0.68 and 0.77, respectively, exhibited more-uniform spherical micellar structures, which is ascribable to their balanced ratios of hydrophilic and hydrophobic blocks. All block copolymers were observed to efficiently solubilize QC, a poorly water-soluble flavonoid; however, encapsulation efficiency is affected by the length of the sugar chain, which highlights the importance of carefully selecting the length of the sugar chain to

maintain well-defined micelle integrity and highly efficient drug encapsulation, which are crucial for effective pharmaceutical formulations and drug-delivery systems.

Data availability

All data supporting the findings of this study are available from the first author (W. Lang) upon reasonable request.

CRediT authorship contribution statement

Weeranuch Lang: conceptualization, investigation, formal analysis, writing–original draft, writing–review & editing. Tomohisa Watanabe: conceptualization, data curation, and formal analysis. Chaehun Lee: formal analysis and validation. Takayoshi Tagami, Feng Li, Takuya Yamamoto, Kenji Tajima: resources and supervision. Redouane Borsali: conceptualization, writing–review and editing. Kenji Takahashi: resources and funding acquisition. Toshifumi Satoh: writing–review & editing, supervision, resources. Takuya Isono: writing–review & editing, conceptualization, supervision, funding acquisition, and project administration.

Acknowledgement

This work was financially supported by the JSPS Fund for the Promotion of Joint International Research (No. 21KK0096), the JST COI-NEXT Program (No. JPMJPF2102) and JST PREST (No. JPMJPR23N2) and JST ASPIRE for Rising Scientists (No. JPMJAP2333), and Photoexcitonix Project (Hokkaido University). The synchrotron radiation experiments were performed at beamline BL40B2 of SPring-8 with the approval of the Japan Synchrotron Radiation Research Institute (JASRI) (Proposal No. 2024A0215). We thank Dr. Masanori Yasui and Mr. Toshiaki Ito from the Faculty of Agriculture for their technical electron-microscopy support. We thank Editage (www.editag.jp) for English language editing.

Declaration of competing interest

The authors declare that they have no competing financial interests or personal relationships that may have influenced the work reported in this paper.

References

Akiba, I., & Sakurai, K. (2021). Characterizing block-copolymer micelles used in nanomedicines via solution static scattering techniques. *Polymer Journal*, 951–973. https://doi.org/10.1038/s41428-021-00489-9

Alenazi, N. A., Bokhari, M. G., Abourehab, M. A. S., & Abukhadra, M. R. (2023). Drug polymeric carrier of aceclofenac based on amphiphilic chitosan micelles. *ACS Omega*, *8*, 48145–48158.

https://doi.org/10.1021/acsomega.3c07065

Allen, C., Maysinger, D., & Eisenberg, A. (1999). Nano-engineering block copolymer aggregates for drug delivery. *Colloids and Surfaces B: Biointerfaces*, *16*, 3–27. https://doi.org/https://doi.org/10.1016/S0927-7765(99)00058-2

Argudo, P. G., Spitzer, L., Cramail, H., Camacho, L., & Lecommandoux, S. (2022). Design and self-assembly of sugar-based amphiphiles: spherical to cylindrical micelles. *Langmuir*, *38*, 7535–7544. https://doi.org/10.1021/acs.langmuir.2c00579

Atanase, L. I. (2021). Micellar drug delivery systems based on natural biopolymers. *Polymers*, *13*(3), 1–33. https://doi.org/10.3390/polym13030477

Bhalani, D. V, Nutan, B., & Kumar, A. (2022). Bioavailability enhancement techniques for poorly aqueous soluble drugs and therapeutics. *Biomedicines*, *10*(2055), 1–33. https://doi.org/10.3390/biomedicines10092055

Cabral, H., Miyata, K., Osada, K., & Kataoka, K. (2018). Block copolymer micelles in nanomedicine applications. *Chemical Reviews*, *118*, 6844–6892. https://doi.org/10.1021/acs.chemrev.8b00199

Chen, K., Chen, C., Chen, H., Komaki, R., Kawakami, N., & Isono, T. (2023). Self-assembly behavior of sugar-based block copolymers in the complex phase window modulated by molecular architecture and configuration. *Macromolecules*, *56*, 28–39. https://doi.org/10.1021/acs.macromol.2c01929

Cushen, J. D., Shanmuganathan, K., Janes, D. W., Willson, C. G., & Ellison, C. J. (2014). Synthesis of amphiphilic naturally-derived oligosaccharide-block-wax oligomers and their self-assembly. *ACS Macro Lett.*, *3*, 839–844. https://doi.org/org/doi/10.1021/mz500389g

Dal Bó, A. G., Soldi, V., Giacomelli, F. C., Travelet, C., Jean, B., Pignot-paintrand, I., Borsali, R., & Fort, S. (2012). Self-assembly of amphiphilic glycoconjugates into lectin-adhesive nanoparticles. *Langmuir*, *28*, 1418–1426. https://doi.org/10.1021/la204388h

Faisal, S., K., Clulow, J., A., Krasowska, M., Gillam, T., Miklavcic, J., S., Williamson, H., N., & Blencowe, A. (2022). Interrogating the relationship between the microstructure of amphiphilic poly (ethylene glycol-b-caprolactone) copolymers and their colloidal assemblies using non-interfering techniques. *Journal of Colloid And Interface Science*, *606*, 1140–1152. https://doi.org/10.1016/j.jcis.2021.08.084

Fulmer, G. R., Miller, A. J. M., Sherden, N. H., Gottlieb, H. E., Nudelman, A., Stoltz, B. M., Bercaw, J. E., & Goldberg, K. I. (2010). NMR chemical shifts of trace impurities: Common laboratory solvents, organics, and gases in deuterated solvents relevant to the organometallic chemist. *Organometallics*, *29*(9), 2176–2179. https://doi.org/10.1021/om100106e

Gao, Y., Wang, Y., Ma, Y., Yu, A., Cai, F., Shao, W., & Zhai, G. (2009). Formulation optimization and in situ absorption in rat intestinal tract of quercetin-loaded microemulsion. *Colloids and*

Surfaces B: Biointerfaces, *71*(2), 306–314. https://doi.org/10.1016/j.colsurfb.2009.03.005

Gauche, C., Soldi, V., Fort, S., Borsali, R., & Halila, S. (2013). Xyloglucan-based diblock co-oligomer: Synthesis, self-assembly and steric stabilization of proteins. *Carbohydrate Polymers*, *98*(2), 1272–1280. https://doi.org/10.1016/j.carbpol.2013.07.064

Ghezzi, M., Pescina, S., Padula, C., Santi, P., Del Favero, E, Cantù, L., & Nicoli, S. (2021). Polymeric micelles in drug delivery: An insight of the techniques for their characterization and assessment in biorelevant conditions. *Journal of Controlled Release*, *332*(February), 312–336. https://doi.org/10.1016/j.jconrel.2021.02.031

Giacomelli, C., Schmidt, V., Aissou, K., & Borsali, R. (2010). Block copolymer systems: from single chain to self-assembled nanostructures. *Langmuir*, *26*(7), 15734–15744. https://doi.org/10.1021/la100641j

Halila, S., Manguian, M., Fort, S., Cottaz, S., Hamaide, T., Fleury, E., & Driguez, H. (2008). Syntheses of well-defined glyco-polyorganosiloxanes by “click” chemistry and their surfactant properties. *Macromolecular Chemistry and Physics*, *209*(12), 1282–1290. https://doi.org/10.1002/macp.200700629

Hansen, S. (2000). Bayesian estimation of hyperparameters for indirect Fourier transformation in small-angle scattering research papers. *Journal of Applied Crystallography*, *33*(1985), 1415–1421. https://doi.org/10.1107/S0021889800012930

Hato, M., Minamikawa, H., Tamada, K., Baba, T., & Tanabe, Y. (1999). Self-assembly of synthetic glycolipid/water systems. *Advances in Colloid and Interface Science*, *80*(3), 233–270. https://doi.org/10.1016/S0001-8686(98)00085-2

Isono, T., Komaki, R., Kawakami, N., Chen, K., Chen, H. L., Lee, C., Suzuki, K., Ree, B. J., Mamiya, H., Yamamoto, T., Borsali, R., Tajima, K., & Satoh, T. (2022). Tailored solid-state carbohydrate nanostructures based on star-shaped discrete block co-oligomers. *Biomacromolecules*, *23*(9), 3978–3989. https://doi.org/10.1021/acs.biomac.2c00813

Isono, T., Komaki, R., Lee, C., Kawakami, N., Ree, B. J., Watanabe, K., Yoshida, K., Mamiya, H., Yamamoto, T., Borsali, R., Tajima, K., & Satoh, T. (2020). Rapid access to discrete and monodisperse block co-oligomers from sugar and terpenoid toward ultrasmall periodic nanostructures. *Communications Chemistry*, *3*(1), 1–9. https://doi.org/10.1038/s42004-020-00385-y

Isono, T., Miyachi, K., Satoh, Y., Nakamura, R., Zhang, Y., Otsuka, I., Tajima, K., Kakuchi, T., Borsali, R., & Satoh, T. (2016). Self-assembly of maltoheptaose-block-polycaprolactone copolymers: carbohydrate-decorated nanoparticles with tunable morphology and size in aqueous media. *Macromolecules*, *49*, 4178–4194. https://doi.org/10.1021/acs.macromol.6b00781

Jacques, D. A., Guss, J. M., Svergun, D. I., & Trewhella, J. (2012). Publication guidelines for

819 structural modelling of small-angle scattering data from biomolecules in solution. *Acta*
820 *Crystallographica Section D: Biological Crystallography*, *68*(6), 620–626.
821 https://doi.org/10.1107/S0907444912012073
822 Janado, M., & Yano, Y. (1985). Hydrophobic nature of sugars as evidenced by their differential
823 affinity for polystyrene gel in aqueous media. *Journal of Solution Chemistry*, *14*(12), 891–902.
824 https://doi.org/10.1007/BF00646298
825 Lang, W., Kumagai, Y., Habu, S., Sadahiro, J., Tagami, T., Okuyama, M., Kitamura, S., Sakairi, N.,
826 & Kimura, A. (2022). Physicochemical functionality of chimeric isomaltomegalosaccharides
827 with α-(1 → 4)-glucosidic segments of various lengths. *Carbohydrate Polymers*, *291*(April),
828 119562. https://doi.org/10.1016/j.carbpol.2022.119562
829 Lang, W., Mondol, D., Trakooncharoenvit, A., Tagami, T., Okuyama, M., Hira, T., Sakairi, N., &
830 Kimura, A. (2023). Formulation and evaluation of a novel megalomeric microemulsion from
831 tamarind seed xyloglucan-megalosaccharides for improved high-dose quercetin delivery.
832 *Food Hydrocolloids*, *137*(December 2022), 108430.
833 https://doi.org/10.1016/j.foodhyd.2022.108430
834 Lang, W., Tagami, T., Kumagai, Y., Tanaka, S., Kang, H. J., Okuyama, M., Saburi, W., Mori, H.,
835 Hira, T., Lee, C., Isono, T., Satoh, T., Hara, H., Kurokawa, T., Sakairi, N., Yuguchi, Y., &
836 Kimura, A. (2023). Tunable structure of chimeric isomaltomegalosaccharides with double α-
837 (1 → 4)-glucosyl chains enhances the solubility of water-insoluble bioactive compounds.
838 *Carbohydrate Polymers*, *319*(July), 121185. https://doi.org/10.1016/j.carbpol.2023.121185
839 Lang, W., Tagami, T., Kang, H., Okuyama, M., Sakairi, N., & Kimura, A. (2023). Partial
840 depolymerization of tamarind seed xyloglucan and its functionality toward enhancing the
841 solubility of curcumin. *Carbohydrate Polymers*, *307*(December 2022), 120629.
842 https://doi.org/10.1016/j.carbpol.2023.120629
843 Lang, W., Tagami, T., Kumagai, Y., Tanaka, S., Kang, H. J., Okuyama, M., Saburi, W., Mori, H.,
844 Hira, T., Lee, C., Isono, T., Satoh, T., Hara, H., Kurokawa, T., Sakairi, N., Yuguchi, Y., &
845 Kimura, A. (2023). Tunable structure of chimeric isomaltomegalosaccharides with double α-
846 (1 → 4)-glucosyl chains enhances the solubility of water-insoluble bioactive compounds.
847 *Carbohydrate Polymers*, *319*(July), 121185. https://doi.org/10.1016/j.carbpol.2023.121185
848 Liu, X., Tan, X., Rao, R., Ren, Y., Li, Y., Yang, X., & Liu, W. (2016). Self-Assembled
849 PAEEP−PLLA micelles with varied hydrophilic block lengths for tumor cell targeting. *ACS*
850 *Applied Materials and Interfaces*, *8*, 23450–23462. https://doi.org/10.1021/acsami.6b06346
851 Mahajan, H. S., Tyagi, V., Lohiya, G., & Nerkar, P. (2012). Thermally reversible xyloglucan gels as
852 vehicles for nasal drug delivery. *Drug Delivery*, *19*(5), 270–276.
853 https://doi.org/10.3109/10717544.2012.704095
854 Majee, S. B., Avlani, D., & Biswas, G. R. (2016). Non-starch plant polysaccharides:

855 Physicochemical modifications and pharmaceutical applications. *Journal of Applied*
856 *Pharmaceutical Science*, *6*(10), 231–241. https://doi.org/10.7324/JAPS.2016.601033
857 Mazzarino, L., Otsuka, I., Halila, S., Bubniak, L. D. S., Mazzucco, S., Santos-Silva, M. C., Lemos-
858 Senna, E., & Borsali, R. (2014). Xyloglucan-block-poly(ε-caprolactone) copolymer
859 nanoparticles coated with chitosan as biocompatible mucoadhesive drug delivery system.
860 *Macromolecular Bioscience*, *14*(5), 709–719. https://doi.org/10.1002/mabi.201300465
861 Modolon, S. D. M., Otsuka, I., Minatti, E., Borsali, R., & Halila, S. (2012). Sweet block copolymer
862 nanoparticles: Preparation and self-essembly of fully oligosaccharide-based amphiphile.
863 *Biomacromolecules*, *13*(I), 1129–1135. https://doi.org/10.1021/bm3000138
864 Niemann, C., Carpita, N. C., & Whistler, R. L. (1997). Arabinose-containing oligosaccharides from
865 tamarind xyloglucan. *Starch/Staerke*, *49*(4), 154–159.
866 https://doi.org/10.1002/star.19970490407
867 Nitta, Y., Fang, Y., Takemasa, M., & Nishinari, K. (2004). Gelation of xyloglucan by addition of
868 epigallocatechin gallate as studies by rheology and differential scanning calorimetry.
869 *Biomacromolecules*, *5*(4), 1206–1213. https://doi.org/10.1021/bm034526y
870 Piovesana, S., Aita, S. E., Cannazza, G., Capriotti, A. L., Cavaliere, C., Cerrato, A., Guarnaccia, P.,
871 Montone, C. M., & Laganà, A. (2021). In-depth cannabis fatty acid profiling by ultra-high
872 performance liquid chromatography coupled to high resolution mass spectrometry. *Talanta*,
873 *228*(January). https://doi.org/10.1016/j.talanta.2021.122249
874 Plucinski, A., Willersinn, J., Lira, R. B., Dimova, R., & Schmidt, B. V. K. J. (2020). Aggregation
875 and crosslinking of poly(N,N-dimethylacrylamide)-b-pullulan double hydrophilic block
876 copolymers. *Macromolecular Chemistry and Physics*, *221*(13).
877 https://doi.org/10.1002/macp.202000053
878 Schatz, C., & Lecommandoux, S. (2010). Polysaccharide-containing block copolymers: Synthesis,
879 properties and applications of an emerging family of glycoconjugates. *Macromolecular Rapid*
880 *Communications*, *31*(19), 1664–1684. https://doi.org/10.1002/marc.201000267
881 Selby, K., & Maitland, C. C. (1967). The cellulase of *Trichoderma viride*. Separation of the
882 components involved in the solubilization of cotton. *The Biochemical Journal*, *104*(3), 716–
883 724. https://doi.org/10.1042/bj1040716
884 Su, H., Wang, F., Ran, W., Zhang, W., Dai, W., Wang, H., Anderson, C. F., Wang, Z., Zheng, C.,
885 Zhang, P., Li, Y., & Cui, H. (2020). The role of critical micellization concentration in efficacy
886 and toxicity of supramolecular polymers. *PNAS*, *117*(9), 4518–4526.
887 https://doi.org/10.1073/pnas.1913655117
888 Thoma, J. A., Wright, H. B., & French, D. (1959). Partition chromatography of homologous
889 saccharides on cellulose columns. *Archives of Biochemistry and Biophysics*, *85*(2), 452–460.
890 https://doi.org/10.1016/0003-9861(59)90510-7

Urakawa, H., Mimura, M., & Kajiwara, K. (2002). Diversity and versatility of plant seed xyloglucan. *Trends in Glycoscience and Glycotechnology*, *14*(80), 355–376. https://doi.org/10.4052/tigg.14.355

Vega-vásquez, P., Mosier, N. S., & Irudayaraj, J. (2020). *Nanoscale drug delivery systems: from medicine to agriculture*. *8*(February), 1–16. https://doi.org/10.3389/fbioe.2020.00079

Vinarov, Z., Katev, V., Radeva, D., Tcholakova, S., & Denkov, N. D. (2018). Micellar solubilization of poorly water-soluble drugs: effect of surfactant and solubilizate molecular structure. *Drug Development and Industrial Pharmacy*, *44*(4), 677–686. https://doi.org/10.1080/03639045.2017.1408642

Xie, F., Li, Z., Li, Z., Li, D., Gao, Y., & Wang, B. (2018). Absolute intensity calibration and application at BSRF SAXS station. *Nuclear Instruments and Methods in Physics Research, Section A: Accelerators, Spectrometers, Detectors and Associated Equipment*, *900*(May), 64–68. https://doi.org/10.1016/j.nima.2018.05.026

Zatorska-Plachta, M., Grzegorz, Ł., Maziarz, U., Forys, A., Trzebicka, B., Wnuk, D., Choluj, K., Karewicz, A., Michalik, M., & Jamroz, D. (2021). Encapsulation of curcumin in polystyrene-based nanoparticles-drug loading capacity and cytotoxicity. *ACS Omega*, *6*, 12168–12178. https://doi.org/10.1021/acsomega.1c00867

Zepon, K. M., Otsuka, I., Bouilhac, C., Muniz, E. C., Soldi, V., & Borsali, R. (2015). Glyco-nanoparticles made from self-assembly of maltoheptaose- block -poly(methyl methacrylate): Micelle, reverse micelle, and encapsulation. *Biomacromolecules*, *16*(7), 2012–2024. https://doi.org/10.1021/acs.biomac.5b00443